ACS NANO

ARTICLE

Nanoscale Correlated Disorder in Out-of-Equilibrium Myelin Ultrastructure

Gaetano Campi,[†] Michael Di Gioacchino,[†,‡,§] Nicola Poccia,[‖] Alessandro Ricci,[‡] Manfred Burghammer,[⊥] Gabriele Ciasca,[#] and Antonio Bianconi*,[†,‡,∇]

[†]Institute of Crystallography, CNR, via Salaria, Km 29.300, 00015 Monterotondo Roma, Italy

[‡]Rome International Center for Materials Science Superstripes (RICMASS), Via dei Sabelli 119A, 00185 Roma, Italy

[§]Department of Science, Nanoscience section, Roma Tre University, Via della Vasca Navale 84, 00146 Roma, Italy

[‖]Department of Physics, Harvard University, Cambridge, Massachusetts 02138, United States

[⊥]European Synchrotron Radiation Facility, 6 Rue Jules Horowitz, BP220, 38043 Grenoble Cedex, France

[#]Physics Institute, Catholic University of Sacred Heart, Largo F. Vito 1, 00168 Rome, Italy

[∇]National Research Nuclear University MEPhI (Moscow Engineering Physics Institute), Kashirskoe shosse 31, 115409 Moscow, Russia

ABSTRACT: Ultrastructural fluctuations at nanoscale are fundamental to assess properties and functionalities of advanced out-of-equilibrium materials. We have taken myelin as a model of supramolecular assembly in out-of-equilibrium living matter. Myelin sheath is a simple stable multilamellar structure of high relevance and impact in biomedicine. Although it is known that myelin has a quasi-crystalline ultrastructure, there is no information on its fluctuations at nanoscale in different states due to limitations of the available standard techniques. To overcome these limitations, we have used scanning micro X-ray diffraction, which is a unique non-invasive probe of both reciprocal and real space to visualize statistical fluctuations of myelin order of the sciatic nerve of *Xenopus laevis*. The results show that the ultrastructure period of the myelin is stabilized by large anticorrelated fluctuations at nanoscale, between hydrophobic and hydrophilic layers. The ratio between the total thickness of hydrophilic and hydrophobic layers defines the conformational parameter, which describes the different states of myelin. Our key result is that myelin in its out-of-equilibrium functional state fluctuates point-to-point between different conformations showing a correlated disorder described by a Levy distribution. As the system approaches the thermodynamic equilibrium in an aged state, the disorder loses its correlation degree and the structural fluctuation distribution changes to Gaussian. In a denatured state at low pH, it changes to a completely disordered stage. Our results aim to clarify the degradation mechanism in biological systems by associating these states with ultrastructural dynamic fluctuations at nanoscale.

KEYWORDS: out-of-equilibrium biological systems, functional nanoscale fluctuations, supramolecular assembly, myelin, scanning micro X-ray diffraction, correlated disorder, levy distribution
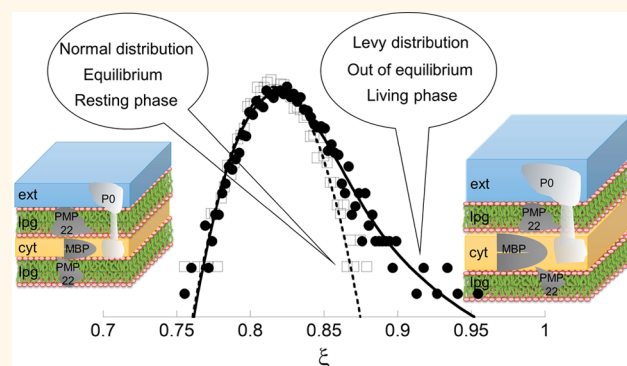
A hot topic for material scientists today is the design of chemical systems in quasi-stationary non-equilibrium states.[1] In fact it is known that chemical systems can acquire novel functionalities such as, for example, chiral symmetry breaking, bistability, and ultimately life,[2] when kept away from equilibrium. In this context, supramolecular self-assembly is of high interest. It involves multiple weak intermolecular interactions between structural units leading to multiple conformational states with similar energy separated by small potential energy barriers. The interchange among the different structural conformations moves the systems along the complex potential energy landscape, which determines their functionality. Thus, the fluctuations between the nearly isoenergetic conformations constitute a key point to be investigated for a deeper understanding of out-of-equilibrium matter, that occurs in biomaterials,[3] plants,[4] nanotechnology,[5] and proteins.[6] In particular, the spatial correlation degree of
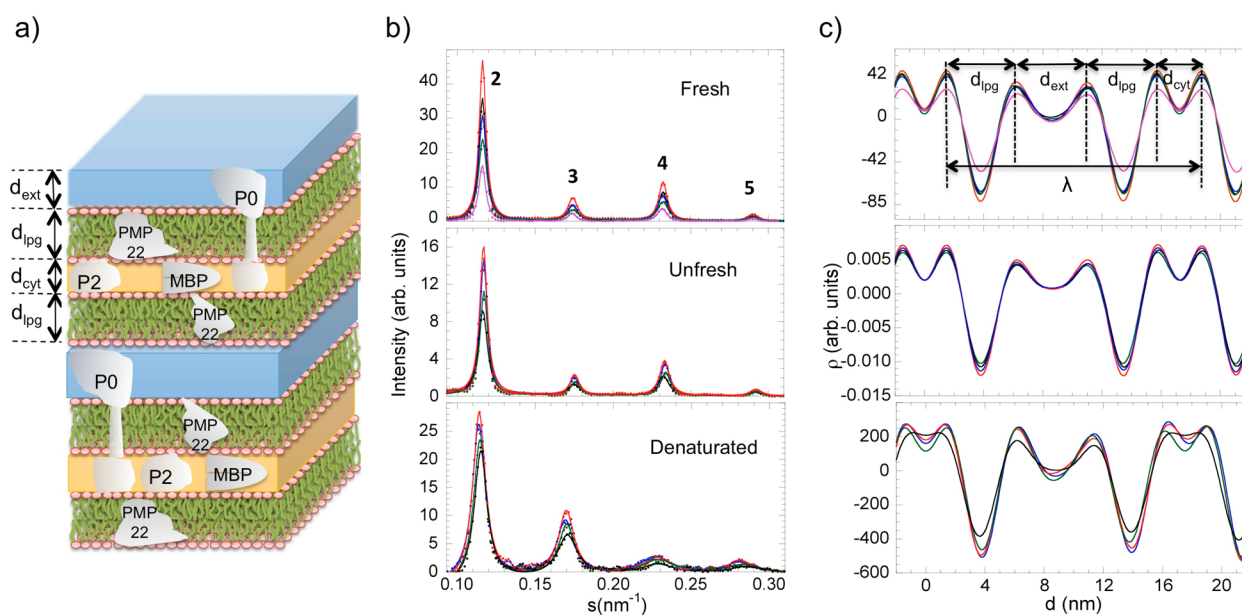
Figure 1. (a) Pictorial view of the myelin membrane layers made of polar lipid groups, *lpg*, with thickness d_{lpg}, intercalated by two hydrophilic layers: the cytoplasmic apposition, *cyt*, and the extracellular apposition, *ext*, with thickness d_{cyt} and d_{ext}, respectively. The location of myelin proteins PMP22, P0, P2, and MBP is indicated. (b) The intensity is plotted against the reciprocal distance, *s*, and the Bragg reflections of order 2, 3, 4, 5 are indicated for each sample. c) The ED distribution has been computed from the diffraction patterns, shown in Figure 1b, using Fourier analysis. The curve presents minima and maxima, with a period $d_\lambda = 2d_{lpg} + d_{ext} + d_{cyt}$, where d_{lpg}, d_{ext}, and d_{cyt} refer to the thickness of lipidic (*lpg*), extracellular (*ext*), cytoplasmatic (*cyt*) zones, respectively. The ED distribution for *unfresh* and *denatured* samples has been obtained in the same way as the other *fresh* one, shown in (b).

these fluctuations defines and characterizes the system thermodynamic state related to its function.

It has been proposed in recent theories that the out-of-equilibrium state of living biological matter is close to a critical point.[7−10] The most significant indicator for proximity to a critical point is critical opalescence where the size of the regions of different phases begin to fluctuate, in a correlated way, over increasingly large length scales.[11] The spatial correlations are described by universal power laws and scaling functions in soft, biological as well as in hard matter.[12−15] Recently the Kaufman group has proposed quantum criticality at origin of life[10] predicting biological matter fluctuations as in a system in proximity to a quantum critical point for metal−insulator transition (MIT). Power law fluctuations in MIT quantum criticality have been well characterized in high-temperature superconductors.[16−19]

Myelin[20,21] can be considered the simplest example of a biological ultrastructure since it shows a periodic multilayer structure rich in phospholipid membranes with few active proteins[22−28] where the competition between fundamental biological interactions[29] determines its quasi-steady-state out-of-equilibrium. The compact myelin sheath is an elaborated multilayered membrane wrapping selected axons. Its main role is the control of the propagation speed of action potentials in saltatory conduction, facilitating nerve signal transmission.[20,21] The myelin ultrastructure is usually described as a highly ordered liquid crystal[22] made of a structural unit constituted by the stacking of the four layers: (i) lipidic membrane (lipid polar group, *lpg*), (ii) cytoplasmatic apposition, *cyt*, (iii) a second lipidic membrane, *lpg*, and (iv) extracellular apposition, *ext*.[27,30] The structural unit appears to be stable, as probed by using a wide variety of standard experimental approaches[25,30−40] giving information only on the average structure and thus inadequate for the visualization of out-of-

equilibrium structural fluctuations, which require highly spatially resolved probes. Besides, on account of the advanced features of the latest generation synchrotron sources and fast acquisition methods, nowadays powerful non-invasive high spatial resolution techniques are available for this purpose.[41,42] In our experimental approach, we have used scanning micro X-ray diffraction (S*μ*XRD) to probe the k-space (reciprocal space) order with high resolution in the real space. In this way we have mapped spatial distribution of myelin ultrastructural fluctuations, for example, the fluctuations of myelin sublayers thickness. In a second step, we have applied statistical physics tools to the collected diffraction data to unveil the "statistical distributions of the fluctuating structural order". This approach has recently been used to carry out heterogeneity investigation of complex matter in several systems of interest in different fields from biomedicine to material science.[26,27,41−43]

We have applied this approach to investigate the myelin in the sciatic nerves of *Xenopus laevis* frogs, which is a peripheral nervous system (PNS) representative. We have measured the spatial fluctuations of the four nanoscale layers thickness at thousands of discrete locations in functional, out-of-equilibrium freshly extracted nerves associated with the *in vivo* state,[33] named *fresh* samples. Afterward, in order to investigate the system degradation toward the thermodynamic equilibrium, we quantified the structural statistical fluctuations of myelin in aged nerves after extraction, named *unfresh*, and *denatured* nerves in acidic pH solution, named *denatured*. We have used the ratio between the thickness of the hydrophilic and hydrophobic layers called hydrophilic−hydrophobic conformational parameter (HhCF) to characterize the myelin local state. We discovered that the quasi-crystalline periodicity of the myelin lattice in the functional state is maintained thanks to large anticorrelated intrinsic fluctuations between the hydrophobic layers and hydrophilic layers. In *fresh* out-of-
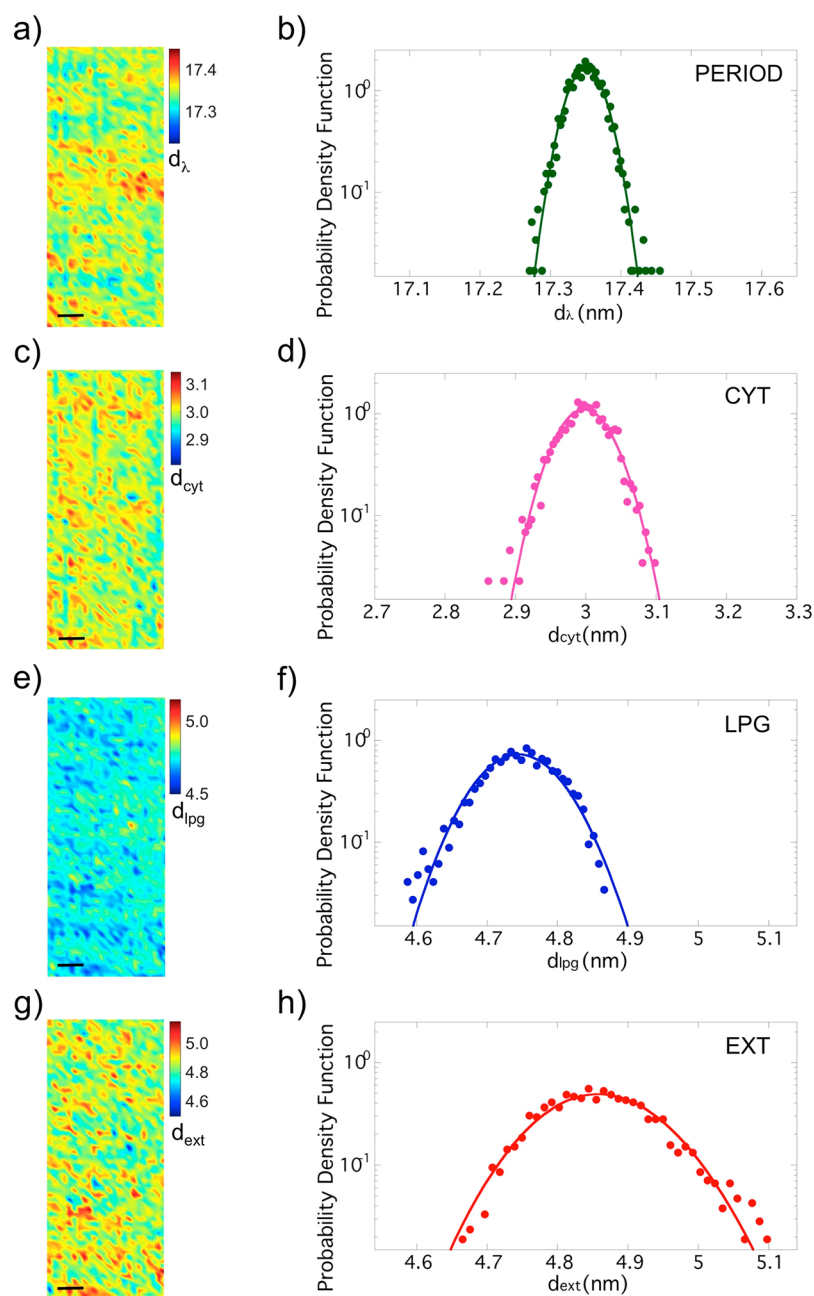
Figure 2. Maps ($300 \times 125 \ \mu m^2$) of d_λ, d_{cyt}, d_{lpg}, and d_{ext} in (a), (c), (e), and (g), respectively. The PDFs of these thickness maps are shown in (b), (d), (f), (h). We notice the larger fluctuations of d_{cyt}, d_{ext}, and d_{lpg} given by $\sigma(d_{cyt})$, $\sigma(d_{ext})$, and $\sigma(d_{lpg})$, respectively, with respect to $\sigma(d_\lambda)$ fluctuations of the period d_λ (see Table 1).

equilibrium samples, the probability distribution of HhCF shows a fat tail, here described by a Levy distribution,[44−49] as expected for biological matter near a quantum critical point.[10−19,50,51] Leaving the functional out-of-equilibrium state, toward the thermodynamic equilibrium, the myelin degrades. In the aged state, we have observed the freezing ultrastructure fluctuations leading to a narrow Gaussian distribution of HhCF, while in the denatured state,[35] at low pH, we observed a disordered state indicated by the larger uncorrelated fluctuations. These results support the hypothesis that the functional *fresh* nerve is a system in a non-equilibrium steady state tuned close to a critical point.[7−10]

RESULTS AND DISCUSSION

The ultrastructure of myelin is shown schematically in Figure 1a. The repetition of the structural unit, made by the stacking of (i) cytoplasmatic (*cyt*), (ii) lipidic (*lpg*), (iii) extracellular (*ext*), and (iv) another lipidic (*lpg*)[27,32] layers, gives rise to the Bragg peaks well-known in literature.[20,26,30,32] The XRD profiles with the indicated Bragg peaks of order 2, 3, 4 and 5, measured in 1 μm^2 area, of *fresh*, *unfresh*, and *denatured* samples are shown in Figure 1b. The individual thickness of each layer, named d_λ, d_{cyt}, d_{lpg}, d_{ext}, have been extracted from electron density (ED) profiles, for the three samples, *fresh*, *unfresh*, and *denatured*, shown in Figure 1c. These ED profiles have been computed by Fourier analysis of the XRD profiles, as described in detail in the Methods section. Different features

Table 1. Statistical Analysis of the of the Thickness d_{cyt}, d_{ext}, d_{lpg}, and d_λ, in the *Fresh*, *Unfresh*, and *Denatured* with pH = 5 Samples, from the ED Profiles for *Xenopus laevis* Sciatic Nerves[a]

samples	μ(nm)			σ(nm)			RSD (%)		
	fresh	*unfresh*	pH = 5	*fresh*	*unfresh*	pH = 5	*fresh*	*unfresh*	pH = 5
d_{cyt}	2.999	2.957	2.832	0.036	0.028	0.237	1.20	0.95	8.37
d_{ext}	4.860	4.797	5.597	0.082	0.049	0.292	1.68	1.03	5.22
d_{lpg}	4.746	4.798	4.669	0.055	0.034	0.256	1.15	0.71	5.49
d_λ	17.350	17.350	17.960	0.024	0.021	0.121	0.14	0.12	0.68

[a]Here we report mean values, μ, standard deviations, σ, and RSD = σ/μ.

in XRD and ED peaks shapes are quite evident; this necessitates a spatially resolved study jointly to the application of spatial statistical tools to describe the ultrastructural fluctuations in this system.

To this purpose, we have scanned the different nerves in 300 × 125 μm^2 central regions of interest (ROI) selected along the vertical axis of the nerves. First, we have built the maps of the thickness of structural unit period, d_λ, and of each sublayer, d_{cyt}, d_{lpg}, d_{ext}, in the *fresh* samples, as shown in Figure 2a,c,e,g, respectively. Then, we calculated the probability density function (PDF) of the same quantities (see Figure 2b,d,f,h). The myelin ultrastructural spatial fluctuations have been defined by the relative standard deviation, $RSD_i = \sigma(d_i)/\mu(d_i)$ on the whole ROI, where $\mu(d_i)$ and $\sigma(d_i)$ are the mean value and the standard deviation of the probability distribution for each thickness, d_i, with $i = \lambda$, *cyt*, *ext* and *lpg*.

Let us consider the thickness of the periodic structural unit, d_λ, (Figure 2a,b). Its average value is found to be $\mu(d_\lambda) = 17.35$ nm, in agreement with previous works.[26,30] Its spatial fluctuation, $RSD_\lambda = \sigma(d_\lambda)/\mu(d_\lambda)$, is about 0.14%, quite smaller than the fluctuations for the other individual sublayers having RSDs between 1.1 and 1.7%, as reported in Table 1. Here we meet the "paradox" of myelin quasi-crystallinity due to the smaller spatial fluctuation of period in comparison with the larger sublayers' fluctuations.

To shed light on this paradox, we have studied the correlations between the spatial fluctuations RSD_{lpg}, RSD_{cyt}, and RSD_{ext}. In order to do this, we first calculated the Pearson's correlation coefficients, c_{i-j}, between maps of cytosolic apposition (Figure 2c), extracellular apposition (Figure 2g), lipidic membrane (Figure 2e) (see Table 2). We observed that the spatial fluctuations RSD_{cyt} are smaller than RSD_{ext}, but d_{cyt} and d_{ext} wave together in the same direction, being $c_{cyt-ext}$ positive. On the other hand, fluctuations RSD_{lpg} go in the opposite direction, since $c_{lpg-ext}$ and $c_{cyt-lpg}$ are negative. This means that the lipid membrane fluctuations are strongly anticorrelated with both cytosolic and extracellular layer fluctuations. It is natural to associate this anticorrelation with the anticorrelated dynamics of the myelin proteins.[25,52−55]

In order to describe the point-to-point spatial structural fluctuations in myelin, we have introduced the HhCF

described by the ratio ξ between hydrophilic and hydrophobic layers:

$$\xi = (d_{ext} + d_{cyt})/2d_{lpg} \tag{1}$$

A typical map of ξ measured on the *fresh* samples is shown in Figure 3a. The red spots represent areas where hydrophilic layers are larger, while in the blue spots they become smaller and the thickness of hydrophobic layers increase. The fact that the ξ is always <0.9 demonstrates that myelin has a high lipid content.[20]

The PDF of ξ shows a skewed line shape modeled by using Levy distributions[44] (see Figure 3b). The Levy distributions provide a statistical description of complex signals deviating from normal behavior and in recent years have found increasing interest in several applications in diverse fields.[45−49] The characteristic function of Levy probability distribution is defined by four parameters: stability index α, skewness parameter β, scale parameter γ taking into account the width of the distribution, and location parameter δ with varying ranges of $0 < \alpha \le 2$, $-1 \le \beta \le 1$, $\gamma > 0$, and δ real. We stress the fact that the closed form expressions of density and distribution functions of Levy distributions are not available except for a few particular cases such as the well-known Gaussian distribution where the stability parameter α is 2. Here we have used basic functions in the numerical evaluation of these parameters and goodness of data fitting as described by Liang and Chen.[56] The Levy fitting curve, indicated by the continuous line in Figure 3b, gives a stability index of 1.78 ± 0.02 (<2), a location of 0.82 ± 0.01, a skewness of 1.00 ± 0.05, and a scale parameter γ of 0.014 ± 0.002.

The ultrastructural dynamic fluctuations and the myelin quasi-crystallinity paradox can be seen in a compact and clear way in Figure 3c. Here we show the scatter plot of the relative variations of the layers, $\Delta d_{ext} = d_{ext} - d_{ext}^0$, $\Delta d_{lpg} = d_{lpg} - d_{lpg}^0$, $\Delta d_{cyt} = d_{cyt} - d_{cyt}^0$, and the period, d_λ, as a function of ξ, where d_{ext}^0, d_{lpg}^0, and d_{cyt}^0 are constant values given by 2.2, 3.7, and 2.2 nm, respectively, which are the thicknesses of the membrane units in the protein-free myelin sheath.[25] We observed that the almost total independence of the period from ξ is due to the positive correlations between the fluctuations of hydrophilic

Table 2. Correlation Coefficients c_{i-j} between Maps of the Spatial Fluctuations between the Different Layers i, j = *cyt*, *ext*, and *lpg* in the *Fresh*, *Unfresh*, and pH = 5 Samples[a]

c_{i-j}	d_{cyt}			d_{ext}			d_{lpg}		
samples	*fresh*	*unfresh*	pH = 5	*fresh*	*unfresh*	pH = 5	*fresh*	*unfresh*	pH = 5
d_{cyt}	1	1	1	0.4452	0.3426	0.7283	**−0.6406**	**−0.5293**	**−0.895**
d_{ext}				1	1	1	**−0.9474**	**−0.8290**	**−0.925**
d_{lpg}							1	1	1

[a]Negatively correlated coefficients are indicated in bold. These correlations are well explained by Figure 6 for each sample.

a)

c)

b)
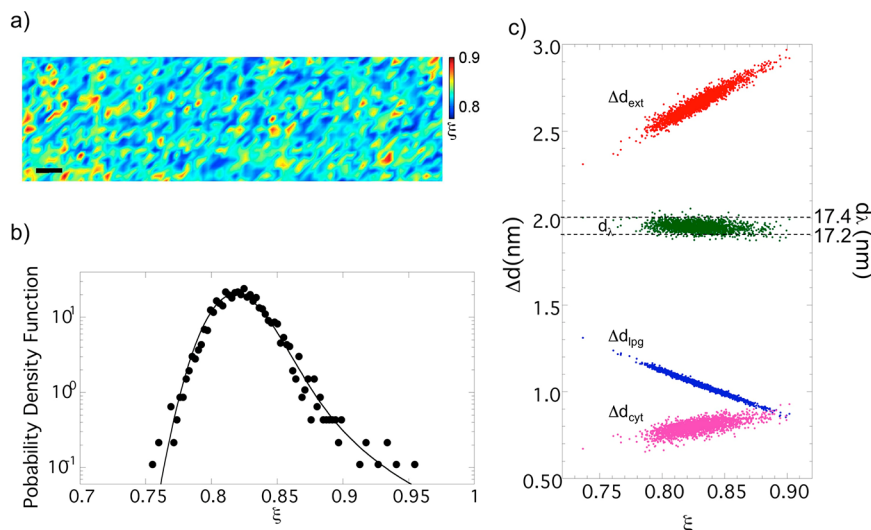
Figure 3. (a) Map of the HhCF conformational parameter, ξ, in a selected central zone of the nerve ($300 \times 125 \ \mu m^2$) and PDF of ξ in semilog plot. Here we notice the fat tail of that PDF fitted with Levy distribution. (b) Scatter plot of absolute dispersion d_λ, $\Delta d_{ext} = d_{ext} - d^0_{ext}$, $\Delta d_{lpg} = d_{lpg} - d^0_{lpg}$, and $\Delta d_{cyt} = d_{cyt} - d^0_{cyt}$ as a function of ξ, where $d^0_{ext} = d^0_{cyt} = 2.2$ nm and $d^0_{lpg} = 3.7$ nm. The period, d_λ, is reported enclosed between two dotted lines at $d_\lambda = 17.4$ nm and $d_\lambda = 17.2$ nm. This plot solves the paradox of the period stability. We note the almost total independence of the period from ξ due to the anticorrelated fluctuations between the hydrophilic layers (*cyt* and *ext*) and the hydrophobic one (*lpg*).

layers (Δd_{ext} and Δd_{cyt}) which increase with increasing ξ, and their anticorrelation with hydrophobic fluctuations, Δd_{lpg}, which decrease with the increase of ξ. This clearly shows that hydrophilic fluctuations compensate the hydrophobic fluctuations to keep the period almost constant giving the apparent static crystalline-like character of the myelin ultra-structure.

Subsequently, we proceeded to check if the described fluctuations are an intrinsic feature of the functional out-of-equilibrium state of myelin, studying the ultrastructural fluctuations in the two different following cases:

(1) An aged state, named *unfresh*, where the sciatic nerve has been left for 18 h in a Ringer solution after the dissection, without insertion of adenosyne-triphosphate (ATP) and oxygen where the system is expected to go toward an equilibrium state from its functional stationary state out-of-equilbrium

(2) A state with acid pH (pH = 5), named *denatured*, where the sciatic nerve has been left in an acid buffer solution where the system is expected to go toward degeneration[35]

The ultrastructural fluctuations of the *unfresh* and *denatured* samples are shown in Figure 4. Typical maps and the PDF of the d_λ, d_{cyt}, d_{lpg}, and d_{ext} thicknesses of the *unfresh* nerve are shown respectively in Figure 4a−d. The dashed lines represent the PDF of the thicknesses in the functional *fresh* nerve, for comparison. The average *unfresh* myelin period, $d_\lambda = 17.350 \pm 0.021$ nm, results are the same as in the *fresh* state. This indicates that the myelin is not yet in any morphologically degenerate state where the period is expected to change significantly.[26,30] On the other hand, we observe significant change in the dynamics of the system. Indeed, both the standard deviations and the mean values of each individual layer thickness change in comparison with the *fresh* functional state. In particular, the spatial fluctuations decrease significantly, as we can see by comparing the RSD values in Table 1. We observe that the lipidic hydrophobic thickness, d_{lpg}, reaches

smaller values down to about 4.6 nm in the *fresh* functional state in comparison with the *unfresh* state. At the same time the hydrophilic extracellular layer reaches larger values up to 5.1 nm in the *fresh* nerve, while it does not exceed 5 nm in the *unfresh* state. The decreasing fluctuations in the *unfresh* nerve are accompanied by the reduction of the spatial correlations, as indicated by comparing the correlation coefficients between cytosolic, extracellular, and lipidic membrane apposition in Table 2. Thus, although the average period in the aged *unfresh* nerve is unchanged, we find (i) decreasing amplitude of fluctuations and (ii) decreasing spatial correlations between fluctuations. The myelin frozen fluctuations support the hypothesis that the aged system has reached a more static state, approaching the thermodynamic equilibrium.

Let us now consider the *denatured* sample at pH = 5. The maps and the relative PDFs of the d_λ, d_{cyt}, d_{lpg}, and d_{ext} thicknesses are shown in Figure 4e−h, respectively. The period PDF (Figure 4e) shows a clear increase in both its mean value and its standard deviation compared to the *fresh* sample. In this case $\mu(d_\lambda) = 17.960$ and $\sigma(d_\lambda) = 0.121$ nm give spatial fluctuations RSD$(d_\lambda) = 0.68\%$, much larger than fluctuations in both *fresh* and *unfresh* states. This is an expected degradation sign of the morphology, indeed, as is commonly known, the degeneration leads to an increase in the period and later breaking of the biological membrane.[30,40]

Alongside the morphologically changes, we observed also dramatic changes in the dynamics of the system. Upon inspection of Figure 4f−h we notice a huge increase of the range of spatial fluctuations for all sublayers, compared to the *fresh* sample. Indeed, now the RSD assume values including between 5.2 and 8.4%, (see Table 1). The PDFs now assume a non-analytic shape, a sign of the sample denaturation process. In particular, focusing our attention on cytosolic apposition PDF (Figure 4f), we can see that there is a long PDF tail at low values of d_{cyt}, which reaches the range of the minimum possible *cyt* thickness.[25] On the contrary, a sharp drop of PDF is visible at high values of d_{cyt}. In order to check the correlation between each sublayer in the *denatured* sample, we direct our attention
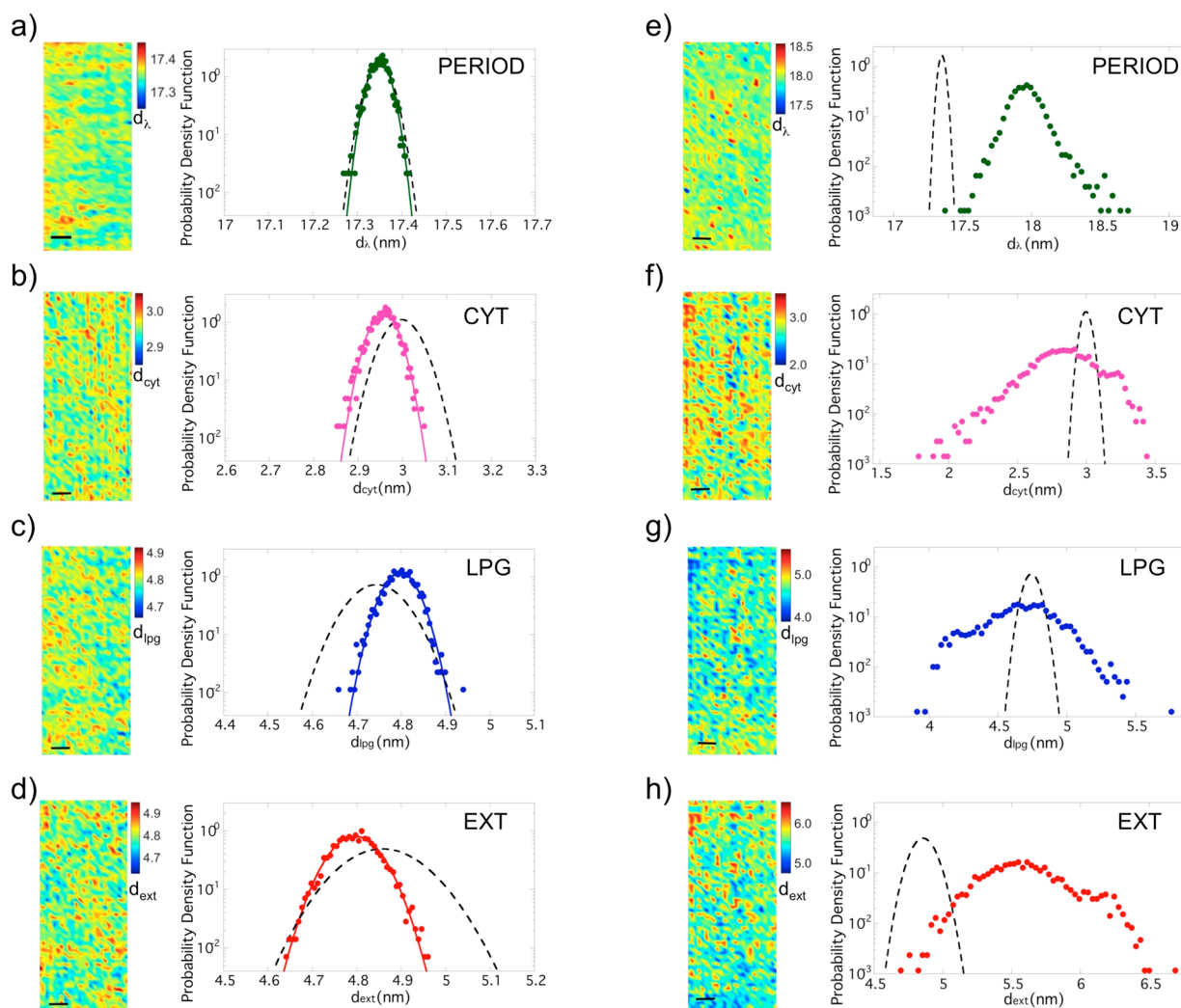
Figure 4. Maps ($300 \times 125 \ \mu m^2$) of d_λ, d_{cyt}, d_{lpg}, and d_{ext} with measured PDF in the *unfresh* sample, depicted in (a−d), while in (e−h) the maps and relative measured PDFs for the *denatured* sample. The dashed lines represent the *fresh* sample in comparison with the other sample. In the *unfresh* sample, despite the unchanged period, in comparison with the *fresh* nerve, we observed reduced fluctuations of d_{cyt}, d_{ext}, and d_{lpg} (see RSD values in Table 1). These narrower fluctuations are associated with the loss of correlated disorder, as can be seen by the decreasing of the Pearson's correlation coefficient for the *unfresh* nerve in Table 2. The case of denaturation with pH shows bigger increasing of fluctuations (see RSD values in Table 1), and the distribution cannot be mathematically modeled, showing signs of the degeneration stage.

to Pearson's correlation coefficients, c_{i-j}, between maps of cytosolic apposition (Figure 4f), extracellular apposition (Figure 4h), and lipidic membrane (Figure 4g). We notice a great enhancement of the coefficient $c_{cyt-ext}$ and a great decreasing of the coefficient $c_{cyt-lpg}$ that shows the correlation and the anticorrelation between the cytosolic apposition and the other two sublayers, in comparison with *fresh* state (see Table 2). At any rate, the bigger coefficient is the anticorrelation $c_{ext-lpg}$, which is however just a little lower than the *fresh* state. Therefore, in general, the sign of coefficient c_{i-j} between sublayers in each sample are maintained, suggesting that these correlations are a structural property more than functional. The structural anticorrelation occurs between d_{lpg} and d_{ext}. This is important because it means that the degradation leads to loss of fluctuations compensation between the myelin forming layers and to the initial dismantling of the layers, but not to the loss of anticorrelation between layers.

Our main result can be illustrated by comparing the PDF of the conformational parameter, ξ maps, in the *fresh*, *unfresh*, and *denatured* samples, shown in Figure 5a,b, respectively. The dashed lines represent the PDF of ξ in the functional *fresh* nerve. Focusing our attention on Figure 5a, we note that the PDF becomes Gaussian in the *unfresh* nerve, losing the fat tail and the correlated disorder at the nanoscale, modeled by Levy flight in the *fresh* sample. Indeed, the stability parameter here becomes equal to 2.00 ± 0.02. Furthermore, there is a decrease of both the location parameter $\delta = 0.81 \pm 0.01$ and of the scale parameter $\gamma = 0.013 \pm 0.002$ compared to the *fresh* sample, which identifies the narrowing of hydrophilic and the increasing of hydrophobic layers.

Regarding the pH = 5 sample, as for the individual sublayers, the PDF of ξ does not follow any clear specific trends, showing the sign of disordering in the denaturation process. There is a substantial expansion of the distribution, associated with an increase in mean value and fluctuation around it. It results in $\xi = 0.9 \pm 0.3$ that shows a great denaturation because it allows
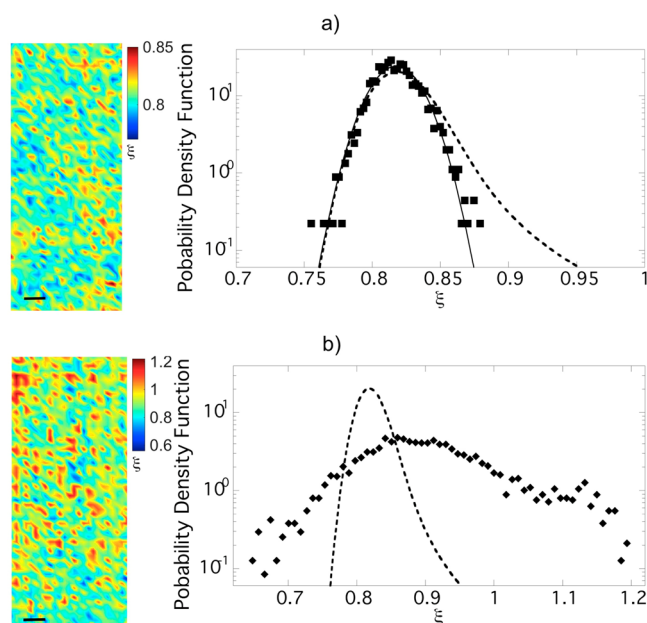
Figure 5. (a) Map of the conformational parameter, ξ, in a selected central zone of the *unfresh* nerve ($300 \times 125\ \mu m^2$) and PDF of ξ in the *unfresh* sample (squared) in semilog plot. The Levy PDF curve found in the *fresh* sample (dashed line) is also reported, for comparison. We notice the loosing of the fat tail in the distribution assuming a Gaussian profile in the *unfresh* sample. (b) Maps ($300 \times 125\ \mu m^2$) of the conformational parameter ξ at the pH = 5 sample and PDF in semilog plot. The dashed line indicates the fit of the *fresh* sample with Levy distribution fat tail. The *denatured* PDF is not fitted because it is not easily mathematically descript and changes shape. The parameter ξ is useful to characterize the overall myelin state uniquely. The map scale bar corresponds to 25 μm.

values of ξ larger than 1, changing the lipid-rich myelin structure in standard physiological form to the lipid-poor myelin with a greater amount of the hydrophobic part in degenerated state.

Finally, the ultrastructural fluctuations in these two non-functional states can be summarized by visualizing the relative variations of the layers, Δd_{ext}, Δd_{lpg}, Δd_{cyt} and the period, d_{λ}, as a function of ξ. The changes in the aged sample are visualized in Figure 6a, where we have compared the relative variations in *unfresh* and in *fresh* samples. Despite the maintained stability of the period, the aged nerve is characterized by (i) decreasing fluctuations and (ii) decreasing spatial correlations between fluctuations. This means that the aged system acquires rigidity and order, losing correlated disorder. This is quite intriguing since it tells us that in the living system, the functionality is associated with the correlated disorder, while the aged state shows the tendency toward a frozen-like state expected at equilibrium with major rigidity and order.

Upon inspection of Figure 6b, the *denatured* pH = 5 sample shows a huge increase of fluctuations of all layers thicknesses. It is worth noting two points: First, the anticorrelative dispersion between the hydrophilic and hydrophobic layers of the structure is maintained. Second, ξ reaches extreme values of 1.22 and 0.66 indicating the coexistence of very poor and very rich lipid phases, respectively. Near $\xi = 1$, we observe the intersection among d_{lpg} and d_{cyt} dispersions, signaled by a dashed line. This marks that the functional state $0.7 < \xi < 0.9$
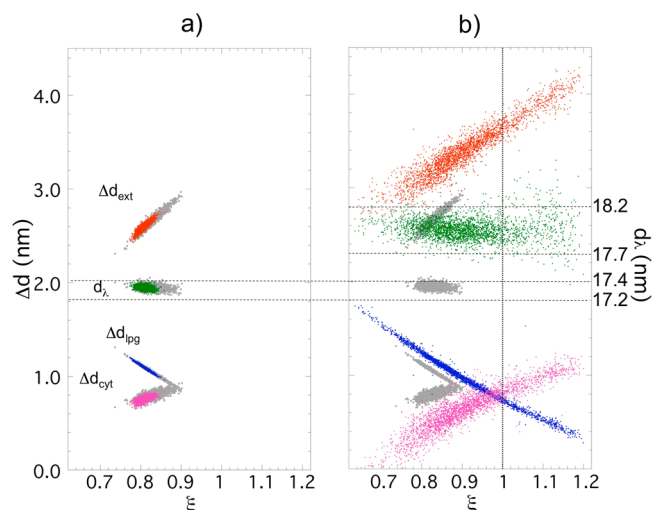
Figure 6. (a) Scatter plot of the period d_{λ} and the dispersions Δd_{ext}, Δd_{lpg}, and Δd_{cyt} (defined in Figure 4) as a function of ξ for the *unfresh* sample. The period fluctuations are enclosed between two dotted lines at $d_{\lambda} = 17.4$ nm and $d_{\lambda} = 17.2$ nm. We notice the loss of fluctuations of each layer and the maintained stability of the period. The gray solid circles representing the fluctuations found in the *fresh* nerve are reported for comparison. (b) Scatter plot of absolute variation Δd_{ext}, Δd_{lpg}, Δd_{cyt}, and d_{λ} as a function of ξ for *denatured* sample. The period is reported on the right axis between two dotted lines at $d_{\lambda} = 18.2$ nm and $d_{\lambda} = 17.7$ nm. The gray solid circles representing the fluctuations found in the *fresh* nerve are reported for comparison. The period results are a little bit increased, while the fluctuations have a great increase, changing the pH. The fluctuations of the hydrophilic layers (*cyt* and *ext*) and the hydrophobic one (*lpg*) are anticorrelated, that is, the *denatured* sample maintains the anticorrelation of the functional state. However, in (b), there is an cross between the membrane dispersion and cytosolic apposition dispersion near $\xi = 1$, that reports the passage to a degraded state, where the period shows a large disorder indicated by the larger spread of period values for $\xi > 1$.

coexists in the degraded states with two class of domains: one lipid-rich region characterized by low HhCF values ($\xi < 0.7$) and a lipid-poor region characterized by high HhCF values ($\xi > 0.9$). In the lipid-poor region, the period dispersion shows a larger disorder, indicated by the larger spread of period values of about the 20%, in comparison with functional and lipid-rich domains.

As a final point, we propose a brief discussion of our achievements. First of all, it is known that, the myelin sublayers are kept together by van der Waals (induced dipole–induced dipole) forces which ensure the integrity and stability of myelin structure.[24] In particular, the fluctuations of each sublayer are due to its protein composition. Indeed, the active dynamics of these proteins cause the various contractions and expansions of each sublayers.

With aging and the denaturation with pH, the myelin loses this dynamic functional ability. The results show a loss of protein dynamic fluctuations[25,53−55] in the *unfresh* sample, as expected, owing to the decreasing ATP content. In fact ATP provides the energy to the myelin, controlling its functionality.[57,58]

For the *denatured* sample, the acid pH (pH = 5) rebalances the van der Waals interactions, which manifests in the variation of the sublayers mean values (d_{cyt}, d_{lpg}, d_{ext}). We remark that the mean value of the hydrophobic layers remains almost

constant compared with the *fresh* state. On the contrary, the hydrophilic layers show large changes of their mean values: The cytosolic apposition narrows and the extracellular apposition increase, in agreement with its behavior in the swollen nerve state,[34] as reported in Table 1.

CONCLUSIONS

We have obtained information on spatial nanoscale fluctuations of out-of-equilibrium PNS myelin ultrastructure of the sciatic nerve of frog *Xenopus laevis* using non-invasive SµXRD imaging. This technique allowed us to map the nanometric fluctuations of the myelin subcomponents: the cytoplasmic, lipidic, and extracellular layers. From statistical analysis we got the following main results: (i) The quasi-crystalline stationary periodicity of the myelin lattice is due to large intrinsic anticorrelated fluctuations of hydrophobic and hydrophilic sublayers, controlled by dynamics of their proteins, and (ii) the local structure of myelin is described by the hydrophobic—hydrophilic conformational parameter HhCF given by the ratio ξ between of the sum of the thickness of two hydrophilic layers (extracellular and cytoplasmatic sublayers) and the sum of the two hydrophobic lipid membranes. We have found that the myelin structural fluctuations are characterized by regions of high hydrophobic content (small HhCF values) with rare events of more hydrophilic regions (large HhCF values) in the functional myelin, *fresh* state. In this sample, the hydrophobic—hydrophilic conformational parameter HhCF follows a Levy distribution with a fat-tail indicating the correlated disorder in the myelin functional biological state, which we associate with the quasi-stationary state in non-equilibrium tuned close to a critical point.[7−10] This is the key result of this work. This assignment is supported by the experimental data for the aged phase where the structural fluctuations are frozen, losing the correlated disorder, and the HhCF distribution changes to a narrow Gaussian centered around $\xi = 0.8$ which is peculiar of a static state approaching equilibrium. Moreover, the Levy distribution disappears also in the denatured state, reached at low pH, where myelin supramolecular structure at nanoscale shows an incoherent disorder. We observe both domains with a large increase of the thickness of the extracellular hydrophilic layers with very large values $\xi > 1$ on one side and on the other extreme there are domains where ξ approaches the minimum possible value ∼0.595 given by the attraction between hydrophobic layers separated by few water layers without proteins,[25] related also with denaturation of the protein structure.

The present results exploit the SµXRD technique to characterize supramolecular chemical structures in quasi-stationary state out of equilibrium. Supramolecular assembly is a robust, rapid, and spontaneous process that it is poorly understood, although it occurs widely in nature, since it takes place in multiple scales and involves very weak intermolecular interactions. The interest in modeling autonomous supramolecular assembly of materials is a vast challenging area in modern material science as well as in basic physical and chemical sciences. Indeed, wide varieties of supramolecular structures are possible depending on the nature of weak forces involved in complex materials made of components ranging from micro- to nanostructures. It is interesting to remark that particular spatial distributions of the supramolecular structure fluctuations have been predicted theoretically to promote quantum coherence at high temperatures.[16−19]

The SµXRD jointly with the spatial statistics allows the investigation of quasi-stationary state out of equilibrium,[59−61] where non-Euclidean hyperbolic space could play a key role in phenomena like chiral symmetry breaking,[62] bistability,[63] and high-temperature superconductivity.[64−67]

Furthermore, the determination of the statistical fluctuations of the myelin supramolecular structure can be important for the study of the emergence of neurodegenerative processes. In fact it is possible that the onset of the neurodegenerative process associated with the transition from the functional ultrastructure to the denatured phase could be detected at an early stage by a deviation of structural fluctuations away from the Levy distribution. More specifically, both the decreasing of structural fluctuations at nanoscale and the loss of their spatial correlations constitute a measure of the degeneration degree.

Finally, developing a paradigm based on a fluctuation—function relation, for myelin like in intrinsic disordered proteins[68] and photosynthesis systems,[69] provides insights for further investigations of ultrastructure dynamics *versus* function, by studying time evolution of spatial fluctuations under external factors such as diseases and drug response.

METHODS

The experimental methods were carried out in accordance with the approved guidelines. Adult female frogs (*Xenopus laevis*; 12 cm length, 180−200 g weight, *Xenopus* express, France) were housed and euthanized at the Grenoble Institute of Neurosciences with kind cooperation of Dr. Andre Popov. The local committee of Grenoble Institute of Neurosciences approved the animal experimental protocol. The frogs were individually transferred in water to a separate room for euthanasia that was carried out using a terminal dose of tricaine (MS222) by immersion; terminal anesthesia was confirmed by the absence of reflexes. Death was ensured by decapitation. Two sciatic nerves were ligated with sterile silk sutures and extracted from both thighs of freshly sacrificed *Xenopus* frogs at approximately the same proximal-distal level through a careful dissection of the thigh. After dissection, the sciatic nerves were equilibrated in culture medium at pH 7.3 for at least 3 h at room temperature. The culture medium was a normal Ringer's solution, containing 115 mM NaCl, 2.9 mM KCl, 1.8 mM CaCl$_2$, and 5 mM HEPES (4−2-hydroxyethyl-1-piperazinyl-ethanesulfonic). Following equilibration, one of the freshly extracted nerves was immediately placed in a thin-walled quartz capillary, 1 mm diameter, sealed with wax and mounted perpendicular to the sample holder, for the SµXRD imaging measurements. In total we acquired 20301 X-ray diffraction patterns for the *fresh* sample.

Another sciatic nerve, after dissection, was left in a Petri dish and equilibrated in culture medium at pH 7.3 for 18 h at room temperature. Following equilibration in the same described conditions, the nerve was prepared for a further SµXRD imaging session on the same day. In total we acquired 8989 X-ray diffraction patterns for the *unfresh* sample.

The third sciatic nerve, after equilibration, was placed in a solution at pH 5 for 3 h at room temperature. The culture acidic solution was an acetate buffer solution, made up by mixing 847 mL of 0.1 M acetic acid (CH$_3$COOH) and 153 mL of 0.1 M sodium acetate trihydrate. Following equilibration, the nerve was placed in a thin-walled quartz capillary, sealed with wax, and mounted on the sample holder for a third SµXRD imaging session. In total we acquired 10201 X-ray diffraction patterns for the *denatured* with pH sample.

The scanning micro X-ray diffraction measurements of myelin of frog's sciatic nerve were performed on the ID13 beamline[26,27] of the European Synchrotron Radiation Facility, ESRF, France. The source of the synchrotron radiation beam is a 18 mm period in vacuum undulator. The beam is first monochromatized by a liquid nitrogen cooled Si-111 double monochromator (DMC) and then is focused by a Kirkpatrick—Baez mirror system. This optic produces an energy X-

ray beam of λ=12.6 KeV on a 1×1 μm^2 spot. The sample holder hosts the capillary-mounted nerve with the horizontal (y) and vertical (z) translation stages with 0.1 μm repeatability. The sample was scanned by using a step size of 5 μm in both y and z directions, in order to avoid a sample damaging and autocorrelation between measured points. A fast readout low noise (FReLoN) camera (1024 × 1024 pixels of 100×100 μm^2) was placed at a distance of 565.0 mm from the sample to collect the 2-D diffraction pattern in transmission. Diffraction images were calibrated using silver behenate powder ($AgC_{22}H_{43}O_2$), which has a fundamental spacing of d_{001} = 58.38 Å. We choose an exposure time of 300 ms for minimizing the radiation damage and keeping good photon counting statistics at the same time.[26,27] The crossed bundle is of approximately 50 myelinated axons. Therefore, the diffraction frames are an average of these axons. Considering the scale of our problem, this is an acceptable average.

We measured different ROIs in the central part of the nerves around their axes to minimize the capillary geometry effect on the X-ray absorption. A typical 2-D diffraction pattern with the expected arc-rings corresponding to the Bragg diffraction orders h = 2, 3, 4, 5 is shown in Figure 1b. The 2-D diffraction patterns have been radially integrated to provide 1-D intensity profiles, $I(s)$, versus transfer moment $s = 2\sin(\theta)/\lambda$, after background subtraction and normalization with respect to the impinging beam (Figure 1b). The 1-D radial profile shows the four characteristic peaks of myelin modeled with a Lorentian line shape from which we get the peak amplitude, $A(h)$, and full width at half height, $w(h)$, used for the Fourier's analysis yielding an ED for each pixel according to

$$|F(h)| = \sqrt{hA(h)w(h)} = \sqrt{hI(h)} \qquad (2)$$

for each reflection of order h. These structure factors, $|F(h)|$, were employed in a Fourier analysis to extract the electron density distribution (EDD) of myelin:

$$\rho = \frac{F(0)}{d} + \left(\frac{2}{d}\right)\sum_{h_{min}}^{h_{max}} \pm F(h/d)\cos(2\pi rh/d) \qquad (3)$$

where the phases were taken from literature:[30,32]

$$F(h) = |F(h)|e^{i\phi_h} = \pm|F(h)| \qquad (4)$$

since the nerve is a centrosymmetric structure, so we consider just the real terms of Fourier series.

The EDD obtained from the diffraction patterns measured at different sample positions in Figure 1b is shown in Figure 1c. From the differences between two adjacent maxima in the EDD profile, the widths of the intermembrane spaces at the cytoplasmic (d_{cyt}) and extracellular (d_{ext}) appositions and the thickness of the lipid bilayer (d_{lpg}) were obtained. From these we got the period of the structural unit[26,32] $d_\lambda = 2d_{lpg} + d_{ext} + d_{cyt}$. A scheme of the myelin ultrastructure is shown in Figure 1a. The extrapolation of EDD at each pixel of the ROI was performed using a customized in-house developed code written in MatLab (Mathworks, Natick, MA).

AUTHOR INFORMATION

Corresponding Author

*E-mail: antonio.bianconi@ricmass.eu.

ORCID

Antonio Bianconi: 0000-0001-9795-3913

Author Contributions

M.B. provided the XRD station at ESRF; N.P. prepared the samples; M.D.G., G.C., A.B., and A.R. performed the data analysis; and G.C, M.D.G., and A.B. wrote the paper.

Notes

The authors declare no competing financial interest.

REFERENCES

(1) van Esch, J. H.; Klajn, R.; Otto, S. Chemical Systems Out of Equilibrium. *Chem. Soc. Rev.* **2017**, *46*, 5474−5475.

(2) Goldenfeld, N.; Woese, C. Life Is Physics: Evolution of a Collective Phenomenon Out of Equilibrium. *Annu. Rev. Condens. Matter Phys.* **2011**, *2*, 375.

(3) Williams, D. *Essential Biomaterials Science*; Cambridge University Press: Cambridge, UK, 2014.

(4) Turner, P.; Nottale, L. The Physical Principles Underpinning Self-Organization in Plants. *Prog. Biophys. Mol. Biol.* **2017**, *123*, 48−73.

(5) Sitharam, M. *Modeling Autonomous Supramolecular Assembly*; Springer: Berlin, 2014; pp 197−216.

(6) Frauenfelder, H.; Sligar, S. G.; Wolynes, P. G. The Energy Landscapes and Motions of Proteins. *Science* **1991**, *254*, 1598−1603.

(7) Mora, T.; Bialek, W. Are Biological Systems Poised at Criticality? *J. Stat. Phys.* **2011**, *144*, 268−302.

(8) Coleman, P. Frontier at Your Fingertips. *Nature* **2007**, *446*, 379.

(9) Poccia, N.; Ansuini, A.; Bianconi, A. Far from Equilibrium Percolation, Stochastic and Shape Resonances in the Physics of Life. *Int. J. Mol. Sci.* **2011**, *12*, 6810−6833.

(10) Vattay, G.; Salahub, D.; Csabai, I.; Nassimi, A.; Kaufmann, S. A. Quantum Criticality at the Origin of Life. *J. Phys.: Conf. Ser.* **2015**, *626*, 012023.

(11) Tauber, U. C. *Scale Invariance in non-Equilibrium Systems, Chapter Part II*; Cambridge University Press: Cambridge, UK, 2013.

(12) Albert, R. Scale-Free Networks in Cell Biology. *J. Cell Sci.* **2005**, *118*, 4947−4957.

(13) Egu'iluz, V. M.; Chialvo, D. R.; Cecchi, G. A.; Baliki, M.; Apkarian, A. V. Scale-Free Brain Functional Networks. *Phys. Rev. Lett.* **2005**, *94*, 018102.

(14) Bonifazi, P.; Goldin, M.; Picardo, M. A.; Jorquera, I.; Cattani, A.; Bianconi, G.; Represa, A.; Ben-Ari, Y.; Cossart, R. GABAergic Hub Neurons Orchestrate Synchrony in Developing Hippocampal Networks. *Science* **2009**, *326*, 1419−1424.

(15) Altamura, M.; Elvevag, B.; Campi, G.; De Salvia, M.; Marasco, D.; Ricci, A.; Bellomo, A. Toward Scale-Free Like Behavior Under Increasing Cognitive Load. *Complexity* **2012**, *18*, 38−43.

(16) Fratini, M.; Poccia, N.; Ricci, A.; Campi, G.; Burghammer, M.; Aeppli, G.; Bianconi, A. Scale-Free Structural Organization of Oxygen Interstitials in La2CuO4+y. *Nature* **2010**, *466* (7308), 841−844.

(17) Poccia, N.; Fratini, M.; Ricci, A.; Campi, G.; Barba, L.; Vittorini-Orgeas, A.; Bianconi, G.; Aeppli, G.; Bianconi, A. Evolution and Control of Oxygen Order in a Cuprate Superconductor. *Nat. Mater.* **2011**, *10* (10), 733−736.

(18) Poccia, N.; Ricci, A.; Campi, G.; Fratini, M.; Puri, A.; Di Gioacchino, D.; Marcelli, A.; Reynolds, M.; Burghammer, M.; et al. Optimum Inhomogeneity of Local Lattice Distortions in La2CuO4+y. *Proc. Natl. Acad. Sci. U. S. A.* **2012**, *109* (39), 15685−15690.

(19) Campi, G.; Bianconi, A.; Poccia, N.; Bianconi, G.; Barba, L.; Arrighetti, G.; Innocenti, D.; Karpinski, J.; Zhigadlo, N. D.; et al. Inhomogeneity of Charge-Density-Wave Order and Quenched Disorder in a High-Tc Superconductor. *Nature* **2015**, *525*, 359−362.

(20) Quarles, R. H., Mcklin, W. B.; Morell, P. Myelin Formation, Structure and Biochemistry. In *Basic Neurochemistry*, 6th ed.; Siegel,

G. J., Agranoff, B. W., Alberts, R. W., Fisher, S. K., Uhler, M. D., Eds; Lippincott-Raven Publishing: Philadelphia, PA, 2006; pp 51−71.

(21) Fields, R. D. Myelin-More Than Insulation. *Science* **2014**, *344*, 264−266.

(22) Peddireddy, K.; Kumar, P.; Thutupalli, S.; Herminghaus, S.; Bahr, C. Myelin Structures Formed by Thermotropic Smectic Liquid Crystals. *Langmuir* **2013**, *29*, 15682−15688.

(23) Lee, D. W.; Banquy, X.; Kristiansen, K.; Kaufman, Y.; Boggs, J. M.; Israelachvili, J. N. Lipid Domains Control Myelin Basic Protein Adsorption and Membrane Interactions Between Model Myelin Lipid Bilayers. *Proc. Natl. Acad. Sci. U. S. A.* **2014**, *111*, E768−E775.

(24) Min, Y.; Kristiansen, K.; Boggs, J. M.; Husted, C.; Zasadzinski, J. A.; Israelachvili, J. Interaction Forces and Adhesion of Supported Myelin Lipid Bilayers Modulated by Myelin Basic Protein. *Proc. Natl. Acad. Sci. U. S. A.* **2009**, *106*, 3154−3159.

(25) Knoll, W.; Peters, J.; Kursula, P.; Gerelli, Y.; Ollivier, J.; Demé, B.; Telling, M.; Kemner, E.; Natali, F. Structural and Dynamical Properties of Reconstituted Myelin Sheaths in the Presence of Myelin Proteins MBP and P2 Studied by Neutron Scattering. *Soft Matter* **2014**, *10*, 519−529.

(26) Poccia, N.; Campi, G.; Ricci, A.; Caporale, A. S.; Di Cola, E.; Hawkins, T. A.; Bianconi, A. Changes of Statistical Structural Fluctuations Unveils an Early Compacted Degraded Stage of PNS Myelin. *Sci. Rep.* **2015**, *4*, 5430.

(27) Di Gioacchino, M.; Campi, G.; Poccia, N.; Bianconi, A. Correlated Disorder in Myelinated Axons Orientational Geometry and Structure. *Condens. Matter* **2017**, *2*, 29.

(28) Wang, B.; Zhang, L.; Bae, S. C.; Granick, S. Nanoparticle-Induced Surface Reconstruction of Phospholipid Membranes. *Proc. Natl. Acad. Sci. U. S. A.* **2008**, *105*, 18171−18175.

(29) Israelachvili, J. N.; McGuiggan, P. M. Forces Between Surfaces in Liquids. *Science* **1988**, *241*, 795−800.

(30) Luo, X.; Cerullo, J.; Dawli, T.; Priest, C.; Haddadin, Z.; Kim, A.; Inouye, H.; Suffoletto, B. P.; Avila, R. L.; et al. Peripheral Myelin of Xenopus Laevis: Role of Electrostatic and Hydrophobic Interactions in Membrane Compaction. *J. Struct. Biol.* **2008**, *162*, 170−183.

(31) D'Rozario, M.; Monk, K. R.; Petersen, S. C. Analysis of Myelinated Axon Formation in Zebrafish. *Methods Cell Biol.* **2017**, *138*, 383−414.

(32) McIntosh, T. J.; Worthington, C. R. Direct Determination of the Lamellar Structure of Peripheral Nerve Myelin at Low Resolution (17 Angstroms). *Biophys. J.* **1974**, *14*, 363−386.

(33) Padróoan, R.; Mateu, L. *In Vivo* Structure of Frog Sciatic Nerve Myelin Membranes: An X-Ray Diffraction Study at 13Å Resolution. *J. Neurosci. Res.* **1981**, *6*, 251−260.

(34) Mateu, L.; Luzzati, V.; Vargas, R.; Vonasek, E.; Borgo, M. Order-Disorder Phenomena in Myelinated Nerve Sheaths: II. The Structure of Myelin in Native and Swollen Rat Sciatic Nerves and in the Course of Myelinogenesis. *J. Mol. Biol.* **1990**, *215*, 385−402.

(35) Vonasek, E.; Mateu, L.; Luzzati, V.; Marquez, G.; Vargas, R.; Céspedes, G.; Cotúa, M.; Borges, J. A Reversible Abnormal Form of Myelin: an X-Ray Scattering Study of Human Sural and Rat Sciatic Nerves. *Eur. Biophys. J.* **2001**, *30*, 11−16.

(36) Finean, J. B. Electron Microscope and X-Ray Diffraction Studies of the Effects of Dehydration on the Structure of Nerve Myelin. *J. Cell Biol.* **1960**, *8*, 13−29.

(37) Möbius, W.; Nave, K.-A.; Werner, H. B. Electron Microscopy of Myelin: Structure Preservation by High-Pressure Freezing. *Brain Res.* **2016**, *1641*, 92−100.

(38) Wang, H.; Fu, Y.; Zickmund, P.; Shi, R.; Cheng, J.-X. Coherent Anti-Stokes Raman Scattering Imaging of Axonal Myelin in Live Spinal Tissues. *Biophys. J.* **2005**, *89*, 581−591.

(39) Ducic, T.; Quintes, S.; Nave, K. A.; Susini, J.; Rak, M.; Tucoulou, R.; Alevra, M.; Guttmann, P.; Salditt, T. Structure and Composition of Myelinated Axons: A Multimodal Synchrotron Spectro-Microscopy Study. *J. Struct. Biol.* **2011**, *173*, 202−212.

(40) Inouye, H.; Liu, J.; Makowski, L.; Palmisano, M.; Burghammer, M.; Riekel, C.; Kirschner, D. A. Myelin Organization in the Nodal, Paranodal, and Juxtaparanodal Regions Revealed by Scanning X-Ray Microdiffraction. *PLoS One* **2014**, *9*, e100592.

(41) Campi, G.; Fratini, M.; Bukreeva, I.; Ciasca, G.; Burghammer, M.; Brun, F.; Tromba, G.; Mastrogiacomo, M.; Cedola, A. Imaging Collagen Packing Dynamics During Mineralization of Engineered Bone Tissue. *Acta Biomater.* **2015**, *23*, 309−316.

(42) Hémonnot, C.Y. J.; Reinhardt, J.; Saldanha, O.; Patommel, J.; Graceffa, R.; Weinhausen, B.; Burghammer, M.; Schroer, C. G.; Köster, S. X-Rays Reveal the Internal Structure of Keratin Bundles in Whole Cells. *ACS Nano* **2016**, *10*, 3553−3561.

(43) Liu, A. C. Y.; Tabor, R. F.; de Jonge, M. D.; Mudie, S. T.; Petersen, T. C. Favored Local Structures in Amorphous Colloidal Packings Measured by Microbeam X-Ray Diffraction. *Proc. Natl. Acad. Sci. U. S. A.* **2017**, *114*, 10344−10349.

(44) Fofack, H.; Nolan, J. P. Tail Behavior, Modes and Other Characteristics of Stable Distributions. *Extremes* **1999**, *2*, 39−58.

(45) Chechkin, A. V.; Gonchar, V. Y.; Klafter, J.; Metzler, R. Fundamentals of Lévy Flight Processes. *Adv. Chem. Phys.* **2006**, *133B*, 439−496.

(46) Oświęcimka, P.; Kwapień, J.; Drożdż, S. Wavelet *Versus* Detrended Fluctuation Analysis of Multifractal Structures. *Phys. Rev. E* **2006**, *74*, 016103.

(47) Barthelemy, P.; Bertolotti, J.; Wiersma, D. S. A Lévy Flight for Light. *Nature* **2008**, *453*, 495−498.

(48) Humphries, N. E.; Queiroz, N.; Dyer, J. R. M.; Pade, N. G.; Musyl, M. K.; Schaefer, K. M.; Fuller, D. W.; Brunnscheweiler, J. M.; Doyle, T. K.; et al. Environmental Context Explains Lévy and Brownian Movement Patterns of Marine Predators. *Nature* **2010**, *465*, 1066−1069.

(49) Podobnik, B.; Valentinčič, A.; Horvatić, D.; Stanley, H. E. Asymmetric Lévy Flight in Financial Ratios. *Proc. Natl. Acad. Sci. U. S. A.* **2011**, *108*, 17883−17888.

(50) Honerkamp-Smith, A. R.; Veatch, S. L.; Keller, S. L. An Introduction to Critical Points for Biophysicists; Observations of Compositional Heterogeneity in Lipid Membranes. *Biochim. Biophys. Acta, Biomembr.* **2009**, *1788*, 53−63.

(51) Poccia, N.; Ricci, A.; Innocenti, D.; Bianconi, A. A Possible Mechanism for Evading Temperature Quantum Decoherence in Living Matter by Feshbach Resonance. *Int. J. Mol. Sci.* **2009**, *10*, 2084−2106.

(52) Ozgen, H.; Schrimpf, W.; Hendrix, J.; de Jonge, J. C.; Lamb, D. C.; Hoekstra, D.; Kahya, N.; Baron, W. The Lateral Membrane Organization and Dynamics of Myelin Proteins PLP and MBP are Dictated by Distinct Galactolipids and the Extracellular Matrix. *PLoS One* **2014**, *9*, e101834.

(53) Laulumaa, S.; Kursula, P.; Natali, F. Neutron Scattering Studies on Protein Dynamics Using the Human Myelin Peripheral Membrane Protein p2. *EPJ Web Conf.* **2015**, *83*, 02010.

(54) Steshenko, O.; Andrade, D. M.; Honigmann, A.; Mueller, V.; Schneider, F.; Sezgin, E.; Hell, S. W.; Simons, M.; Eggeling, C. Reorganization of Lipid Diffusion by Myelin Basic Protein as Revealed by STED nanoscopy. *Biophys. J.* **2016**, *110*, 2441−2450.

(55) Stadler, A. M.; Stingaciu, L.; Radulescu, A.; Holderer, O.; Monkenbusch, M.; Biehl, R.; Richter, D. Internal Nanosecond Dynamics in the Intrinsically Disordered Myelin Basic Protein. *J. Am. Chem. Soc.* **2014**, *136*, 6987−6994.

(56) Liang, Y.; Chen, W. A Survey on Computing Levy Stable Distributions and a New MATLAB Toolbox. *Signal Processing* **2013**, *93*, 242−251.

(57) Shin, Y.; Chung, H. J.; Park, C.; Jung, J.; Jeong, N. Adenosine 5′-Triphosphate (ATP) Inhibits Schwann Cell Demyelination During Wallerian Degeneration. *Cell. Mol. Neurobiol.* **2014**, *34*, 361−368.

(58) Jung, J.; Jo, H. W.; Kwon, H.; Jeong, N. Y. ATP Release Through Lysosomal Exocytosis From Peripheral Nerves: The Effect of Lysosomal Exocytosis on Peripheral Nerve Degeneration and Regeneration After Nerve Injury. *BioMed Res. Int.* **2014**, *2014*, 1−6.

(59) Bertini, L.; De Sole, A.; Gabrielli, D.; Jona-Lasinio, G.; Landim, C. Macroscopic Fluctuation Theory for Stationary Non-Equilibrium States. *J. Stat. Phys.* **2002**, *107*, 635−675.

(60) Spohn, H. Long Range Correlations for Stochastic Lattice Gases in a Non-Equilibrium Steady State. *J. Phys. A: Math. Gen.* **1983**, *16*, 4275−4291.

(61) Derrida, B.; Lebowitz, J. L.; Speer, E. R. Free Energy Functional for Non Equilibrium Systems: An Exactly Solvable Case. *Phys. Rev. Lett.* **2001**, *87*, 150601.

(62) Rueckes, T. Carbon Nanotube-Based Nonvolatile Random Access Memory for Molecular Computing. *Science* **2000**, *289*, 94−97.

(63) Kondepudi, D. K.; Kaufman, R. J.; Singh, N. Chiral Symmetry Breaking in Sodium Chlorate Crystallization. *Science* **1990**, *250*, 975−976.

(64) Ricci, A.; Poccia, N.; Campi, G.; Coneri, F.; Barba, L.; Arrighetti, G.; Polentarutti, M.; Burghammer, M.; Sprung, M.; et al. Networks of Superconducting Nano-Puddles in 1/8 doped YBa2Cu3O6.5+y Controlled by Thermal Manipulation. *New J. Phys.* **2014**, *16*, 053030.

(65) Bianconi, A.; Ricci, A. Lattice, Charge, and Spin Phase Inhomogeneity in Complex-Striped Quantum Matter. *J. Supercond. Novel Magn.* **2016**, *29*, 3013−3016.

(66) Turner, P.; Nottale, L. J. A New *Ab Initio* Approach to the Development of High Temperature Superconducting Materials. *J. Supercond. Novel Magn.* **2016**, *29*, 3113.

(67) Campi, G.; Bianconi, A. High-Temperature Superconductivity in a Hyperbolic Geometry of Complex Matter from Nanoscale to Mesoscopic Scale. *J. Supercond. Novel Magn.* **2016**, *29*, 627−631.

(68) Bianconi, A.; Ciasca, G.; Tenenbaum, A.; Battisti, A.; Campi, G. Temperature and Solvent Dependence of the Dynamical Landscape of Tau Protein Conformation. *J. Biol. Phys.* **2012**, *38*, 169−179.

(69) Campi, G.; Ciasca, G.; Poccia, N.; Ricci, A.; Fratini, M.; Bianconi, A. Controlling Photoinduced Electron Transfer Via Defects Self-Organization for Novel Functional Macromolecular Systems. *Curr. Protein Pept. Sci.* **2014**, *15*, 394−399.